Energy 238 (2022) 121856

Contents lists available at ScienceDirect

Energy

journal homepage: www.elsevier.com/locate/energy

An improved thermodynamic model for supersonic real-gas ejectors using the compound-choking theory

Antoine Metsue [a, b, *], Romain Debroeyer [a], Sébastien Poncet [b], Yann Bartosiewicz [a]

[a] Institute Mechanics, Materials, and Civil Engineering (iMMC), Université Catholique de Louvain (UCLouvain), 1348, Louvain-la-Neuve, Belgium
[b] Mechanical Engineering Department, Université de Sherbrooke, 2500 Boulevard de L'Université, Sherbrooke, QC, J1K 2R1, Canada

ARTICLE INFO

Article history:
Received 11 March 2021
Received in revised form
18 August 2021
Accepted 20 August 2021
Available online 24 August 2021

Keywords:
Supersonic ejector
Real gas
Compound-choking
Fabri-choking
Thermodynamic modeling

ABSTRACT

Thermodynamic models constitute one of the essential tools to properly design supersonic ejectors. However, by their simplistic nature, most of said models remain unable to properly integrate the adequate physics that takes place within the device. Most notably, the Fabri-choking theory constitutes the building block of the large majority of those models. However, it has recently been shown that the so-called compound-choking theory may be better suited to predict the behavior of a double choked ejector. In the present study, a new state-of-the-art thermodynamic model based on the compound-choking theory is presented. First, the algorithm of the on- and off-design model is laid out. Then, the link between Fabri- and compound-choking is clarified by comparing the model with its Fabri-choking counterpart. Characteristic curves are calibrated onto air and R134a experimental data. Finally, an analytical study is performed to show that imposing the compound-choking is actually equivalent to maximizing the mass flow rate within the ejector.

© 2021 Elsevier Ltd. All rights reserved.

1. Introduction

Much as they may offer a compelling alternative to traditional compression devices, ejectors are nonetheless characterized by complicated fluid dynamics, and some of the mechanisms at play within the ejector remain insufficiently understood, which hinders the performance of the global system [1]. Though the most straightforward approach to acquire data might be to perform experiments, such a strategy would not be economically advantageous as it would require too much time and material resources [2]. Instead, numerical methods seem to be the most profitable way to generate results. To this end, using thermodynamic models is the easiest and fastest way to give a first rough appreciation of ejector performance and/or to design them.

Ejectors are passive devices used to suck and compress fluids: a primary stream transfers a part of its energy and momentum to a secondary stream through viscous shearing and suction into the low pressure jet, leading to complex turbulent mixing phenomena in the mixing chamber [3]. During this process, the flow goes through a series of oblique shock waves that interact with the shear layer, thus re-compressing the fluid [4]. Because ejectors are used as entrainment devices, a convenient quantity to characterize their performance is their entrainment ratio $\omega = \dot{m}_s/\dot{m}_p$. To outline the different regimes of an ejector, it is convenient to draw its characteristic curves, which depict the evolution of the entrainment ratio as a function of the back-pressure. Fig. 1 depicts a typical ejector characteristic curve. Depending on the operating conditions and on the internal geometry of the ejector, the secondary flow might become choked as well [5]. As a result, below a certain value of the back-pressure, the secondary flow also becomes independent of the upstream conditions. This particular value of the back-pressure at which, given a particular stagnation pressure ratio $p_{p,0}/p_{s,0}$, the secondary flow becomes choked, is referred to as the *critical pressure* denoted by p^*_{out}. This phenomenon also implies that below p^*_{out}, the entrainment ratio becomes constant and the ejector is said to operate in the *on-design* regime or *critical* mode. Above the critical pressure, the ejector is influenced by the back-pressure. When the latter is increased, a shock wave moves into the mixing chamber, interacting with the mixing and boundary layers and hindering the secondary mass flow. The ejector is then said to operate in the *off-design* regime or *sub-critical* mode. If the back-pressure is increased above a threshold value referred to as the *breakdown pressure*, the primary flow reverses back into the suction

* Corresponding author. Institute Mechanics, Materials, and Civil Engineering (iMMC), Université catholique de Louvain (UCLouvain), 1348, Louvain-la-Neuve, Belgium.
E-mail address: antoine.metsue@uclouvain.be (A. Metsue).

https://doi.org/10.1016/j.energy.2021.121856
0360-5442/© 2021 Elsevier Ltd. All rights reserved.

Nomenclature

Alpha numeric symbols

$\dot{m}$	Mass flow rate $[kg.s^{-1}]$
A	Area $[m^2]$
a	Speed of sound $[m.s^{-1}]$
D	Diameter $[m]$
G	Mass flux $[kg.m^{-2}.s^{-1}]$
h	Specific enthalpy $[J.kg^{-1}]$
M	Mach number[-]
p	Pressure $[Pa]$
q	Quality $[-]$
R	Specific gas constant $[J.(kg.K)^{-1}]$
s	Specific entropy $[J.(kg.K)^{-1}]$
T	Temperature $[K]$
V	Velocity $[m.s^{-1}]$
x	Horizontal coordinate $[m]$

Subscripts

0	Stagnation conditions
2	Diffuser inlet
c	Setpoint back pressure
d	Diffuser outlet
e	Primary nozzle exit
guess	Guessed value
h	Hydraulic
is	Isentropic conditions
m	Mixed flow
max	Maximum
N	Normal shock
out	Outlet conditions
p	Primary flow
pol	Polytropic
s	Secondary flow
sat	Saturated vapour conditions
t	Primary throat
w	Wall
y	Hypothetical throat

Superscripts

*	Critical conditions

Greek letters

β	Compound-flow indicator $[m^2]$
η	Efficiency $[-]$
γ	Heat capacity ratio $[-]$
ω	Entrainment ratio $[-]$
ρ	Density $[kg.m^{-3}]$
τ	Shear stress $[kg.m^{-1}.s^{-2}]$
ε	Error tolerance $[-]$

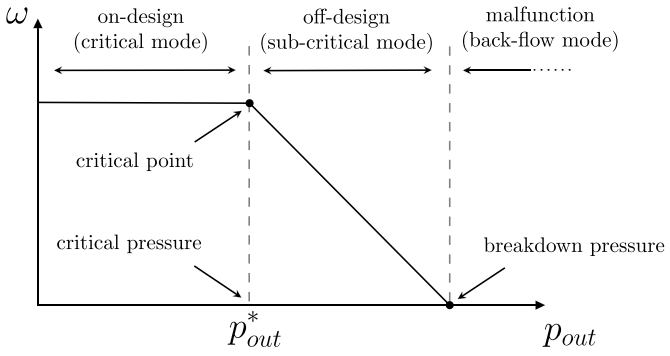

Fig. 1. Typical characteristic curve of an ejector.

chamber. This case corresponds to a malfunction of the ejector. The interested reader can refer to the recent reviews of Besagni et *al.* [6], Ameur et *al.* [7,8] and Grazzini et *al.* [9] for more details about the applications, functioning and modeling of supersonic ejectors.

The first one-dimensional mathematical model of an ejector was introduced by Keenan et *al.* [10] in 1950. It was based on the application of mass, momentum and energy conservation equations, with the use of isentropic flow relations. This model has been used as a theoretical basis in ejector design since then. They compared constant-pressure mixing and constant-area mixing and deduced that the former performed better. However, the model of Keenan et *al.* [10] was unable to provide information on the choking phenomenon at play within a supersonic ejector [11].

Munday and Bagster [12] later proposed modifications to the model of Keenan et *al.* [10]. Their theory assumed that the two streams do not mix right away at the exit of the primary nozzle, but they rather conserve their integrity until a particular downstream section. It was postulated that an hypothetical throat is formed by the primary flow and the ejector wall, and that the secondary stream reaches a sonic velocity at that particular location (Fig. 2). The two streams then mix at constant pressure. This phenomenology is somewhat related to the *choked secondary flow* pattern that was discovered experimentally by Fabri and Siestrunck [13] in 1958. Since the presence of an hypothetical throat constitutes the basis of numerous mathematical models, the choking mechanism associated with this regime is often referred to as *Fabri-choking* [14].

Based on those early works, a number of first generation thermodynamic models were proposed; Eames et *al.* [15] introduced in 1995 a model that included irreversibilities due to friction losses by using isentropic efficiencies; Huang et *al.* [16] developed a model of double-choking that also took irreversibilities into account, but for which they considered that the mixing phenomenon occurred inside the constant area duct; Rogdakis and Alexis [17] introduced a first real gas thermodynamic model with general conservation equations. However, those models could only predict the ejector performance at critical mode operation. In 2013, Chen et *al.* [18] introduced a model to predict the ejector performance at critical and sub-critical operational regimes. Their model was also based on the presence of an hypothetical throat inside the constant area duct. For the sub-critical operating regime, this hypothesis was conserved. The off-design performance was obtained by using a mixing efficiency dependant on the back-pressure of the ejector. Perfect gas behavior was assumed and isentropic efficiencies were used to take friction losses into account. A few years later, Chen et *al.* [2] extended the model to real gas thermodynamic properties.

As pointed out by Lamberts et *al.* [19], the *Fabri-choking* is used as the foundation of most thermodynamic ejector models, including all of the aforementioned models [2,12,15–17,20–23]. However, the Fabri-choking has only been experimentally observed once, by Lamberts et *al.* [14] and characterized by signature shock-wave patterns called lambda-shocks. Indeed, according to the same authors, in many works where on-design ejectors are studied, no

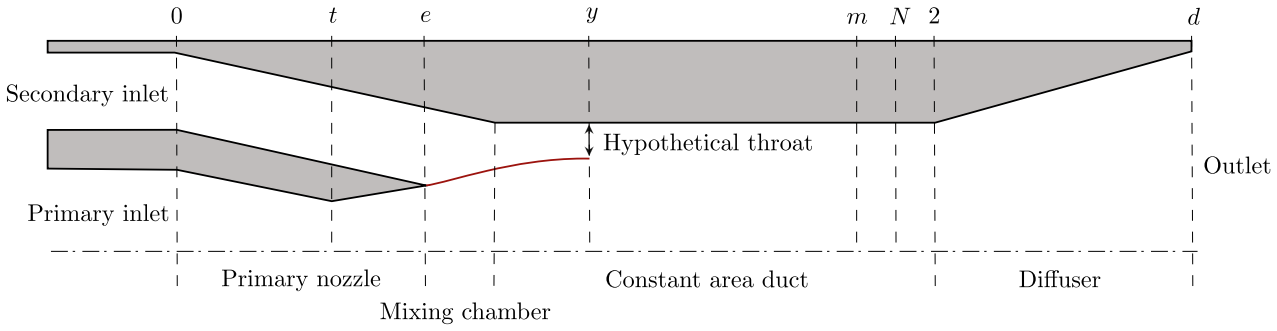

Fig. 2. Schematic diagram of the ejector model (top half).

apparent sonic section in the core of the secondary stream is observed. In addition, significant discrepancies remain between experiments and model predictions, with on-design entrainment ratio deviations up to 16% in Ref. [2], and a reported average deviation of 7.8% in Ref. [24] as two examples. Hence, the Fabri-choking is not necessarily representative of the actual phenomena occurring inside of a doubly choked ejector. In their article, Lamberts et *al.* [19] described a new choking theory for perfect gas based on the early work of Bernstein et *al.* [25] about the so-called *compound-choking* theory. This theory proposed by Lamberts et *al.* [19] for perfect gas ejectors was then extended to real gas ejectors by Fang [26] and Metsue [27] for CFD and thermodynamic modeling purposes, respectively. Very recently, Croquer et *al.* [28] also validated the compound-choking for single-phase gas refrigerants using both approaches. In the latter study, the authors demonstrated, neglecting friction, that the mean error on the predicted entrainment ratio was reduced to about 5% when using the compound-choking criterion, compared to a mean error of more than 17% when using the Fabri-choking criterion.

In the present paper, the compound-choking theory developed by Fang [26] is used for the first time to build a *real gas* thermodynamic model for both on- and off-design operating regimes. First, the ejector model is presented, along with the solving algorithm (Section 3). The model of Chen et *al.* [2] is modified to integrate the compound-choking theory. Then, the new model is used to shed light on the relationship between the Fabri-choking and compound-choking criteria. It is then calibrated on experimental data for supersonic ejectors working with R134a and air, and the results are discussed in details in Section 4. Lastly, it is demonstrated that using the compound-choking criterion is actually equivalent to maximizing the total mass flow rate within the ejector working with a perfect gas (Section 5), which is the physical characteristic of a choked flow. The paper ends by some conclusions and future views in Section 6.

2. Ejector model and solving algorithm

Over the numerous thermodynamic models published in the literature, the model of Chen et *al.* [2] is preferred as a basis for the present research, with some improvements. First, the primary flow is solved by maximizing the mass flow rate instead of imposing a Mach number M equal to unity at the throat, which constitute the primary definition of a choked flow. Most notably, the secondary flow is using the compound-choking theory, instead of the Fabri-choking theory commonly adopted by thermodynamic models.

2.1. Assumptions

The flow within an ejector is quite complex and thus often requires the use of assumptions in order to solve the flow swiftly, which is the essence of thermodynamic models. The main assumptions used in the present work are:

1. The flow is one dimensional, steady and adiabatic. The inlet (primary and secondary) and outlet velocities are supposed to be negligible.
2. Friction losses along the walls and within the shear layer between the primary and secondary streams are taken into account through isentropic efficiencies (Fig. 2): η_p for the primary nozzle (sections $0 \rightarrow e$); $\eta_{p,y}$ for the friction losses undertaken by the primary flow within the mixing chamber (sections $e \rightarrow y$); η_s for the friction losses undertaken by the secondary flow within the mixing chamber (sections $0 \rightarrow y$) and η_d for the diffuser (sections $2 \rightarrow d$). The mixing losses between the primary and secondary streams are taken into account by means of a loss coefficient η_m (sections $y \rightarrow m$).
3. Real gas properties are retrieved from the tabulated database `COOLPROP` available in the Python library.
4. Primary and secondary streams do not start mixing up until a particular section —that will be referred to as *mixing section*— located inside the constant area duct. At that location, both pressures are assumed to be equal. The location of the particular section at which the mixing phenomenon begins is the location of the hypothetical throat that is well described in the literature [11]. This section is *compound-choked* if the ejector is working under critical regime.

A schematic of the ejector, along with the notations that will be used in the following sections, is shown in Fig. 2. Since the primary flow is assumed to be choked, the primary mass flow rate $\dot{m}_p$ is constant and does not depend on any downstream quantity (i.e., it only depends on the primary stagnation conditions). The primary flow expands in the primary nozzle, and then further more in the mixing chamber until it reaches section y. The secondary flow is also —separately— expanded upon section y, and then only the mixing process starts. In other words, the two flows are essentially independent up until reaching section y. It is important to note that the position of the mixing section y is assumed to lie within the constant area section, whether or not the ejector is working in the on- or off-design regime. Then, the two flows start to mix at constant pressure, and are assumed to be completely mixed upon section m. If the flow is supersonic at section m, it consequently goes through a normal shock at section N, located in the constant area section as well. The flow thus reaches the diffuser inlet —section 2— at a subsonic speed. It then further expands in the diffuser, where the flow velocity is further decreased and the pressure recovered.

2.2. Modeling of on-design operation using the compound-choking criterion

2.2.1. Primary nozzle

The flow in the primary nozzle can be solved from the stagnation conditions and the isentropic efficiency governing the flow in this part. It is convenient to set the stagnation conditions with the primary pressure $p_{p,0}$ and the primary temperature $T_{p,0}$. When working with saturated fluids, it is sometimes more relevant to define stagnation conditions with the quality of the fluid $q_{p,0}$. For the sake of simplicity, the stagnation conditions will be defined with $p_{p,0}$ and $T_{p,0}$ in the following.

First, the enthalpy and entropy of the primary flow at the inlet can be computed from the pressure and temperature:

$$h_{p,0} = h(p_{p,0}, T_{p,0}), \tag{1}$$

$$s_{p,0} = s(p_{p,0}, T_{p,0}). \tag{2}$$

For a given pressure p_p and assuming an isentropic expansion, the enthalpy at said pressure can be computed:

$$h_{p,is} = h(p_p, s_{p,0}). \tag{3}$$

Knowing the isentropic efficiency of the primary nozzle η_p, one can then compute the enthalpy resulting from the non-isentropic expansion process:

$$h_p = h_{p,0} - \eta_p \ (h_{p,0} - h_{p,is}). \tag{4}$$

The density along the expansion can then be computed from the pressure and enthalpy. From the conservation of total enthalpy, one can also compute the flow velocity:

$$\rho_p = \rho(p_p, h_p), \tag{5}$$

$$V_p = \sqrt{2 \ (h_{p,0} - h_p)}. \tag{6}$$

In order to solve the flow, the hypothesis of choked primary flow has then to be used. The classical way to impose such a condition is to set the Mach number to unity at the nozzle throat. Although this is the approach taken in the model of Chen *et al.* [2], one prefers to impose the choking condition by the maximization of the mass flux. This approach presents two advantages. First, one does not require to know the speed of sound at the throat for the computation of the primary mass flow rate, which can sometimes be problematic for two-phase flows, as the COOLPROP library is flawed for thermodynamic conditions close to the saturation curve. Then, if one considers a non-isentropic expansion, the sonic section is not actually located at the geometric throat of the nozzle, but rather at a certain distance downstream. Imposing a Mach number equal to unity at the throat would consequently lead to an error in the computation of the primary mass flow rate. By rather directly maximizing the mass flow rate, this problem is avoided and the physical definition of a choked flow is preserved. Indeed, in the case of an isentropic nozzle flow, it can be shown that maximizing the mass flow rate per unit area is equivalent to imposing $M = 1$ at the throat. The mass flux (i.e., the mass flow rate per unit area) is defined as:

$$G = \rho V. \tag{7}$$

From Eq. (1) through (7), the expansion of the fluid in the primary nozzle can be computed. Fig. 3 shows the typical behavior of G along an expansion with R134a as the working fluid for various stagnation conditions. One can observe that the mass flow rate per unit area has a maximum along the expansion. Furthermore, this maximum gets higher and closer to the stagnation pressure as the stagnation temperature gets lower, i.e. the stagnation conditions get to the left hand side of the saturation curve. Indeed, as the temperature gets lower, the fluid transitions from a superheated vapour (for $T_{p,0} = 100$ °C) to a denser subcooled liquid (for $T_{p,0} = 65$ °C and $T_{p,0} = 60$ °C). The much higher density of a liquid explains why the maximum of G gets higher. In addition, one can see that as $T_{p,0}$ gets lower, the maximum of G shifts to the left (i.e., at a pressure closer to the stagnation pressure).

For stagnation conditions where the fluid is highly subcooled, there is actually somewhat of an angular point at the location of the maximum, as the fluid flashes along the expansion. By doing so, the fluid looses a great deal of density in an almost discontinuous fashion. This brings forward the need to compute very accurately the position of the maximum, because due to this angular point, a slight imprecision will lead to a substantial error in the mass flow rate. To compute efficiently the maximum mass flux, it is convenient to use the fact that G has only one maximum. Therefore, one can proceed iteratively by computing $G = f(p_p)$ for a reduced amount of linearly spaced pressures p_p, and then narrowing the interval on p_p where the maximum is located until finding the solution with the desired precision.

Knowing the maximum mass flow rate per unit area $G_{p,max}$ and the throat area of the nozzle A_t, the mass flow rate for the choked primary nozzle is found by:

$$\dot{m}_p = G_{p,max} A_{p,t}. \tag{8}$$

The throat thermodynamic state is then fully solved, as $G_{p,max}$ provides the knowledge of the throat pressure $p_{p,t}$, which can later be used to find the throat enthalpy $h_{p,t}$ by the use of Eqs. (3) and (4). The velocity at the throat is then found using Eq. (6).

It is important to note that the COOLPROP library is faulty near the critical point, meaning that requesting the computation of a thermodynamic quantity near said region generates an error. In order to circumvent this issue and prevent the whole operation to stop, it was chosen to manage this error by assuming that the thermodynamic quantities near the vicinity of the faulty region are equal to the quantities slightly above or slightly below the critical point. Except in the rare case where the maximum of G is located

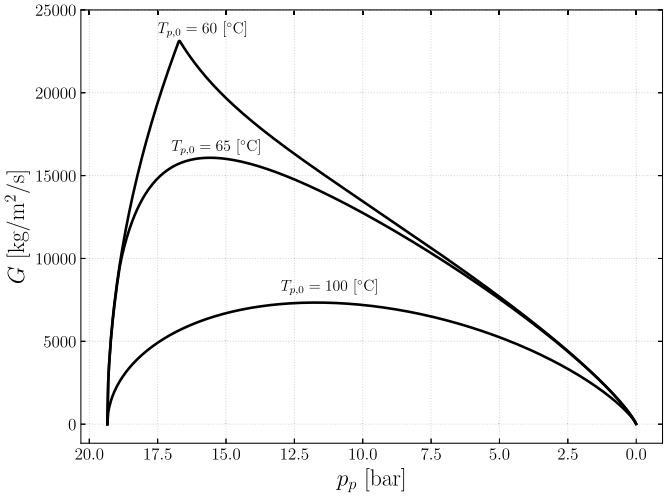

Fig. 3. Variations of the mass flux G as a function of the primary flow pressure p_p for three stagnation temperatures. Results obtained for R134a with $p_{p,0} = 1.934$ [MPa] and $\eta_p = 0.97$.

exactly at the critical point, this procedure does not lead to any loss of accuracy.

The nozzle exit conditions are found by further expanding the flow from the known state at the throat. Knowing the exit section area $A_{p,e}$, the exit state of the fluid is found by using the mass and total enthalpy conservation equations. Indeed, the flow must satisfy:

$$V_{p,e} = \frac{\dot{m}_p}{\rho_p A_{p,e}}, \tag{9}$$

and

$$V_{p,e} = \sqrt{2(h_{p,t} - h_p) + V_{p,t}^2}, \tag{10}$$

where h_p and ρ_p can be computed along the expansion (i.e., as a function of p_p) in the divergent of the nozzle with the use of Eqs. (4) and (5), respectively. The solution $V_{p,e}$ is found by selecting the unique value that allows Eqs. (9) and (10) to be satisfied simultaneously. Once again, the state at the primary nozzle exit is then fully defined, as the value of $V_{p,e}$ provides direct knowledge of $\rho_{p,e}$ and $h_{p,e}$.

2.2.2. Mixing chamber

The on-design conditions at section y (i.e., the mixing section) can be found using the compound-choking criterion for real gas derived in Ref. [28], i.e.:

$$\beta = p_y \left(\frac{A_{p,y}}{\left(\rho_{p,y} V_{p,y}^2\right)} \left(1 - M_{p,y}^2\right) + \frac{A_{s,y}}{\left(\rho_{s,y} V_{s,y}^2\right)} \left(1 - M_{s,y}^2\right) \right) = 0, \tag{11}$$

where the secondary flow properties at section y are computed from the secondary inlet conditions and using the prescribed value of p_y (please refer to Croquer et al. [28] for more details). Once the value of p_y is found with sufficient precision (i.e., $\beta \leq \varepsilon$, with ε the error tolerance), all properties at section y are known, and the secondary mass flow rate can be computed by:

$$\dot{m}_s = \rho_{s,y} V_{s,y} A_{s,y}, \tag{12}$$

which allows to determine the on-design entrainment ratio $\omega = \dot{m}_s / \dot{m}_p$. Fig. 4 shows the flowchart of the algorithm described here. Note that the procedure to compute the critical back pressure will be presented in the next section (i.e., the modeling of the subcritical regime), as it is the same for on- and off-design operations.

2.3. Modeling of off-design operation

Similarly to the previous subsection, the present model is based on the one published by Chen et *al.* [2]. However, their original model suffers from mass conservation issues between sections y and m. Indeed, because said model assumes that the mixing process between primary and secondary flows occurs at a constant pressure, the associated equation (i.e., $p_y = p_m$) is added to the system to solve the flow at section m. However, by doing so, the mass conservation equation is omitted; momentum, energy and pressure constraints are enough to solve the system, resulting in the fact that $\dot{m}_p + \dot{m}_s \neq \rho_m V_m A_y$. To overcome this issue, the present model does not consider that the mixing process occurs at constant pressure. Instead, the mass conservation equation is re-introduced to solve the flow between sections y and m.

Unlike in on-design operation, the off-design ejector performance depends on downstream conditions (i.e., the back pressure p_{out}). Indeed, if the ejector is operating in the off-design regime, information will travel from the end of the diffuser up to the mixing section. The mixing pressure p_y will consequently be higher when the ejector is operating in off-design regime than when it is operating in on-design regime, and the secondary mass flow rate will thereby be impacted. The entrainment ratio will thus be dependant on the back pressure. As mentioned previously for on-design operation, it is not required to solve the flow downstream of section y in order to compute the entrainment ratio. This is not true if one wishes to obtain ω for a particular back pressure. In order to determine the ejector regime and, if necessary, compute the entrainment ratio for off-design operation, the flow has to be solved up to the diffuser exit, i.e. section d (Fig. 2). As a reminder, the condition for the ejector to be in on-design regime is given by:

$$p_{out} < p_{out}^*, \tag{13}$$

where p_{out}^* is the critical back pressure. Hence, the critical back pressure has to be computed to assess the operating regime. First, the thermodynamic states and velocities of the primary and secondary flows are computed using the on-design model, that is, using the compound-choking theory. Then, properties are computed at section m, that is the particular section located inside the constant area duct at which primary and secondary flows are assumed to be completely mixed. State m therefore constitutes one single state, without any distinction between the two flows.

As stated above, the assumption of constant mixing pressure in the original paper of Chen et *al.* [2] is lifted and replaced by the mass conservation equation. This implies that an additional term has to be added to the momentum conservation equation, to take into account the pressure difference between sections m and y. This involves that state m has to be solved using an iterative method, as V_m depends on the unknown pressure p_m. State m is therefore defined by four equations. First, the conservation of mass writes:

$$\rho_m V_m A_y = \dot{m}_p + \dot{m}_s. \tag{14}$$

Then, the momentum conservation equation writes:

$$V_m = \eta_m \frac{\dot{m}_p V_{p,y} + \dot{m}_s V_{s,y} + (p_y - p_m) A_y}{\dot{m}_p + \dot{m}_s}. \tag{15}$$

Note at this point that η_m does not need to be a linear function of p_{out} as it was the case for the model of Chen et *al.* [2]. Instead η_m is assumed to be constant. The third equation is the total enthalpy conservation equation:

$$h_m = \frac{\dot{m}_p h_{p,0} + \dot{m}_s h_{s,0}}{\dot{m}_p + \dot{m}_s} - \frac{V_m^2}{2}, \tag{16}$$

and the last equation is the equation of state linking ρ_m, p_m and h_m:

$$\rho_m = \rho(p_m, h_m). \tag{17}$$

To solve this system of equations, the pressure p_m is guessed. The flow velocity V_m is then computed from Eq. (15), along with the enthalpy h_m using Eq. (16). The flow density ρ_m can then be obtained from Eq. (17). The pressure p_m is modified until Eq. (14) is satisfied. Practically, the solution is found by restraining at each iteration the solution interval on p_m until finding the minimum (or here, also the zero) of $|\rho_m V_m A_y - (\dot{m}_p + \dot{m}_s)|$.

After the mixing, the flow may be or not supersonic. However, it has to be subsonic when entering the diffuser, otherwise it would actually act as a divergent nozzle, thereby accelerating the flow.

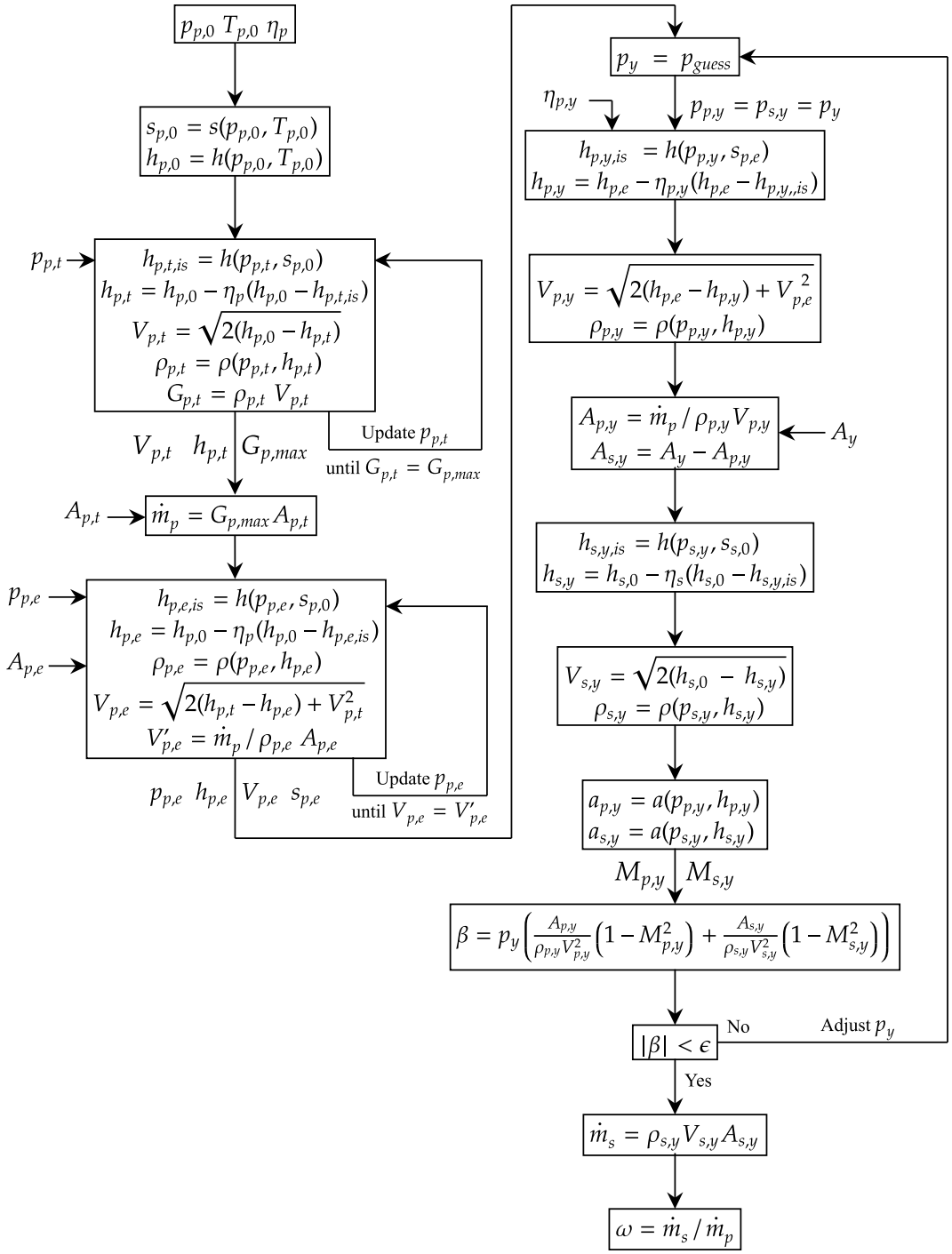

Fig. 4. Flowchart of the model for on-design operations using the compound-choking criterion (Fig. 2).

However, the goal is to recover the pressure at the ejector exit. For the 0-D model, if the flow is supersonic at section *m*, it was chosen to re-compress it through a single normal shock located at the end of the constant area duct (section *N*). Note that sections *m*, *N* and 2 are virtually at the same location, but were drawn separately in Fig. 2 for the sake of readability.

Because the flow may already be subsonic upon section *m*, it was chosen to check the Mach number at said section and compute the normal shock only if $M_m > 1$. Indeed, if the flow at section *m* is subsonic, it is unnecessary to solve the equations for a normal shock. In that case, the subsonic flow at the diffuser inlet (section 2) is indistinguishable from the flow at section *m*. On the other hand, if the flow is indeed supersonic at section *m*, the mass, momentum and total enthalpy conservation equations have to be solved to compute the flow at section 2. This has to be performed using an iterative scheme. First, the fluid density is guessed at section 2:

$$\rho_2 = \rho_{guess}, \tag{18}$$

with ρ_{guess} chosen higher than ρ_m. The flow speed is then computed from the conservation of mass:

$$V_2 = \frac{\rho_m V_m}{\rho_2}, \tag{19}$$

From the conservation of total enthalpy, the enthalpy is computed as:

$$h_2 = h_m + \frac{V_m^2}{2} - \frac{V_2^2}{2}, \tag{20}$$

and the pressure at section 2 is obtained from tabulated data by:

$$p_2 = p(\rho_2, h_2), \tag{21}$$

The momentum conservation equation is then used to update the value of ρ_2 that was initially guessed:

$$\rho_2 = \frac{\left(\rho_m V_m^2 + p_m - p_2\right)}{V_2^2}. \tag{22}$$

The latter value of ρ_2 is then re-injected in Eq. (19) and re-computed until convergence. State 2 being fully defined, the last step is to solve the flow within the diffuser. To this end, one must first retrieve the entropy at section 2 from tabulated data:

$$s_2 = s(p_2, h_2). \tag{23}$$

The enthalpy at the diffuser exit (section d) for an isentropic compression denoted $h_{d,is}$ may be expressed using the classical definition of the isentropic efficiency η_d:

$$\eta_d = \frac{h_{d,is} - h_2}{h_d - h_2}. \tag{24}$$

Then, applying the total enthalpy conservation equation:

$$h_d = h_2 + \frac{V_2^2}{2}, \tag{25}$$

one finally gets:

$$h_{d,is} = h_2 + \eta_d \frac{V_2^2}{2}, \tag{26}$$

where the assumption of negligible flow velocity at section d was used. The pressure at the diffuser exit can finally be computed by:

$$p_d = p(h_{d,is}, s_2), \tag{27}$$

as the end pressure for the isentropic expansion is the same as that of the non-isentropic one. If the ejector is double-choked, the computed pressure p_d actually corresponds to the critical back pressure p^*_{out}, and if the ejector is under sub-critical regime, one has that $p_d = p_{out}$.

For a given back pressure p_c, one can now determine if the ejector works in the on- or off-design regime. For the latter case, the pressure at the end of the diffuser must match the back pressure, which requires to solve the flow in an iterative way until finding the pressure p_y that satisfies:

$$\frac{|p_d - p_c|}{p_c} \leq \varepsilon, \tag{28}$$

with ε the error tolerance. As mentioned previously, the mixing pressure p_y gets higher as the back pressure gets higher when the ejector is working in the off-design regime. Pressure p_y is therefore updated at each iteration until satisfying Eq. (28). Fig. 5 summarizes the computation algorithm of the new off-design model.

3. Validation of the thermodynamic model for single-phase ejectors

3.1. Relation between fabri-choking and compound-choking

It is now proposed to explain in more details the link between Fabri-choking and compound-choking. To do that, the air ejector geometry of the test bench at Université catholique de Louvain and considered by Lamberts et *al.* [14,19] is modeled for $p_{p,0}/p_{s,0} = 4.5$ and with $\eta_m = 0.92$. All other efficiencies are set to 1. First, one can plot the evolution of the mixing pressure as a function of the back pressure as displayed in Fig. 6a. One can notice that the design mixing pressure p^*_y, and therefore the on-design plateau, are higher when using the compound-choking criterion. This can be interpreted as follows: as thoroughly discussed in Ref. [28], the compound-choking predicts the choking of the ejector for secondary Mach numbers lower than 1 at the aerodynamic throat (section y). Hence, the pressure at said location must be higher than that in the case of the Fabri-choking (i.e., $M_{s,y} = 1$) because the secondary flow has been less expanded. In addition, note that as the back pressure tends to the breakdown pressure, the mixing pressure tends to reach the secondary stagnation pressure. As expected, when $p_y = p_{s,0}$, there is no pressure gradient to expand the secondary flow, hence $\dot{m}_s = 0$ and the entrainment ratio gets to zero.

Then, Fig. 6b presents the evolution of the entrainment ratio as a function of the mixing pressure. As a reminder, ω can be computed as a function of the mixing pressure and the stagnation conditions only. Then, the positions of the critical conditions can be located for both choking criteria. Those are represented by dots on the curve. One can now clearly see why the compound-choking criterion systematically predicts higher entraiment ratios than the Fabri-choking criterion. Indeed, the entrainment ratio predicted by the compound-choking is located exactly at the maximum of the curve. This means that, if the transformations are isentropic until the mixing section, satisfying the compound-choking criterion will lead to the maximization of the total mass flow rate within the ejector. Indeed, since the primary flow is choked, maximizing ω is equivalent to maximizing $\dot{m}_s$ and therefore $\dot{m}_p + \dot{m}_s$.

On the other hand, the Fabri-choking mixing pressure at the critical condition p^*_y is slightly lower than that of the maximum. Although not discussed in the article of Chen et *al.* [2], it was found, by re-implementing their model, that because the Fabri-choking criterion does not maximize the entrainment ratio (and thus the total mass flow rate), the near-critical off-design part of the characteristic curve contains a spurious overshoot. Indeed, as one gets further into the off-design part of the characteristic curves, the mixing pressure p_y gets higher. Hence, starting from the Fabri-choking critical point (Fig. 6b) and following the curve towards the right, one eventually reaches the maximum (i.e., the compound-choking critical point). By the same token, it is the authors understanding that other thermodynamic models based on the Fabri-choking criterion and modeling off-design operation should logically present similar overshoots, unless they have been manually cropped. This spurious overshoot will be observed and further discussed in the following.

3.2. Influence of the isentropic efficiencies on the characteristic curves

In order to efficiently calibrate the model, it is relevant to assess the individual effect of each efficiency on the shape of the

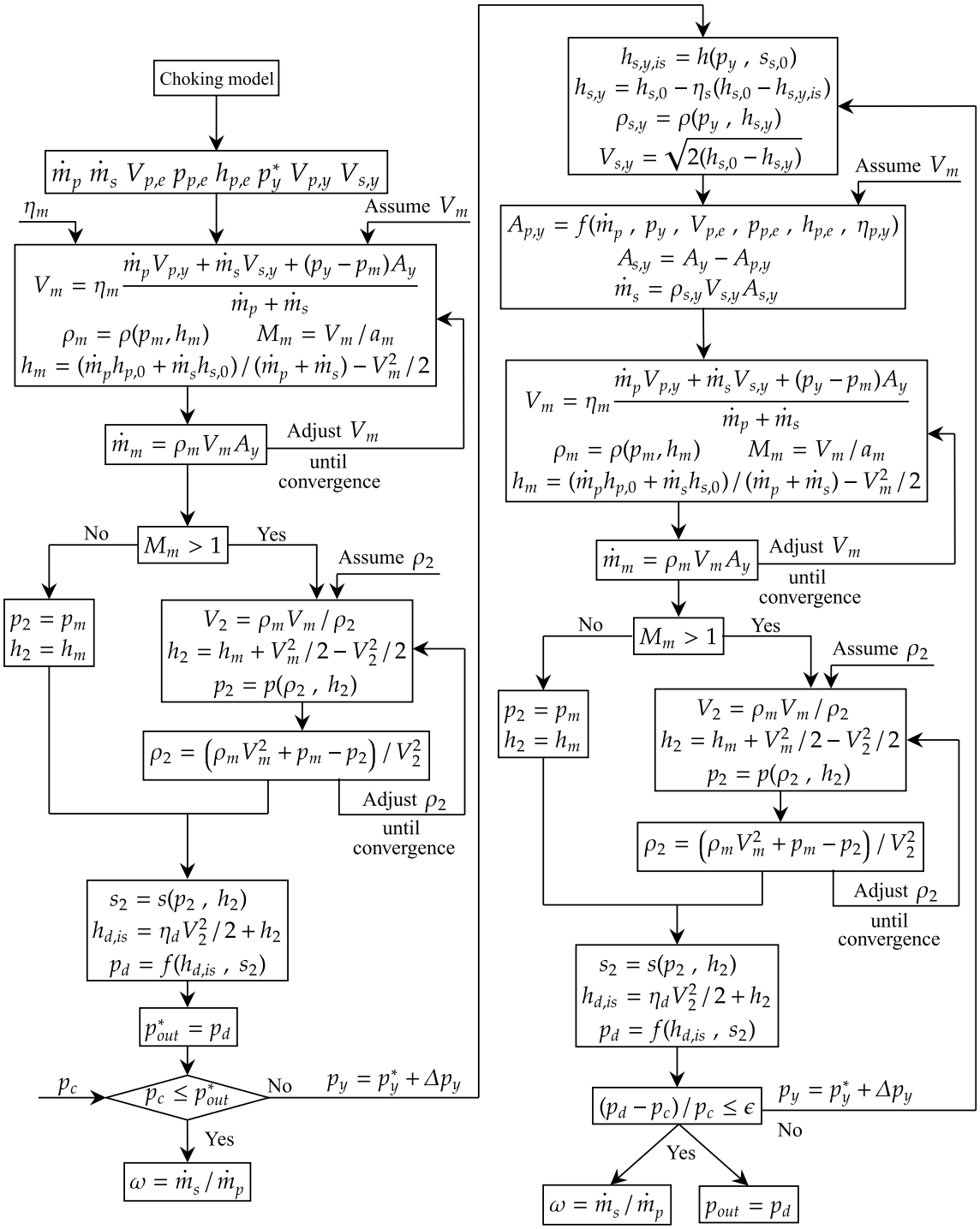

Fig. 5. Flowchart of the model for off-design operation.

characteristic curves by varying one of the efficiencies at a time. Fig. 7 displays the influence of the four isentropic efficiencies (i.e., η_p, η_s, $\eta_{p,y}$ and η_d) and the mixing efficiency η_m. The curves for the counterpart Fabri-choking model (i.e., imposing $M_{s,y} = 1$) have also been displayed for comparison purposes. Note that, if not mentioned, the isentropic efficiencies are set to 1 by default and η_m to 0.95.

One can then observe the influence of the different isentropic efficiencies and the results may be summarized as follows:

- When decreasing η_p, the primary mass flow rate is decreased, as the flow velocity at the primary throat gets lower. The on-design entrainment ratio therefore increases. The effect of friction in the primary nozzle is somewhat equivalent to having a lower primary stagnation pressure. This explains the fact that the critical back pressure gets lower.
- When decreasing η_s, the on-design entrainment ratio gets lower, as the secondary mass flow rate is decreased. The back pressure is closely related to the total mass flux going through the ejector. Thus, a lower secondary mass flow rate also results in a decrease

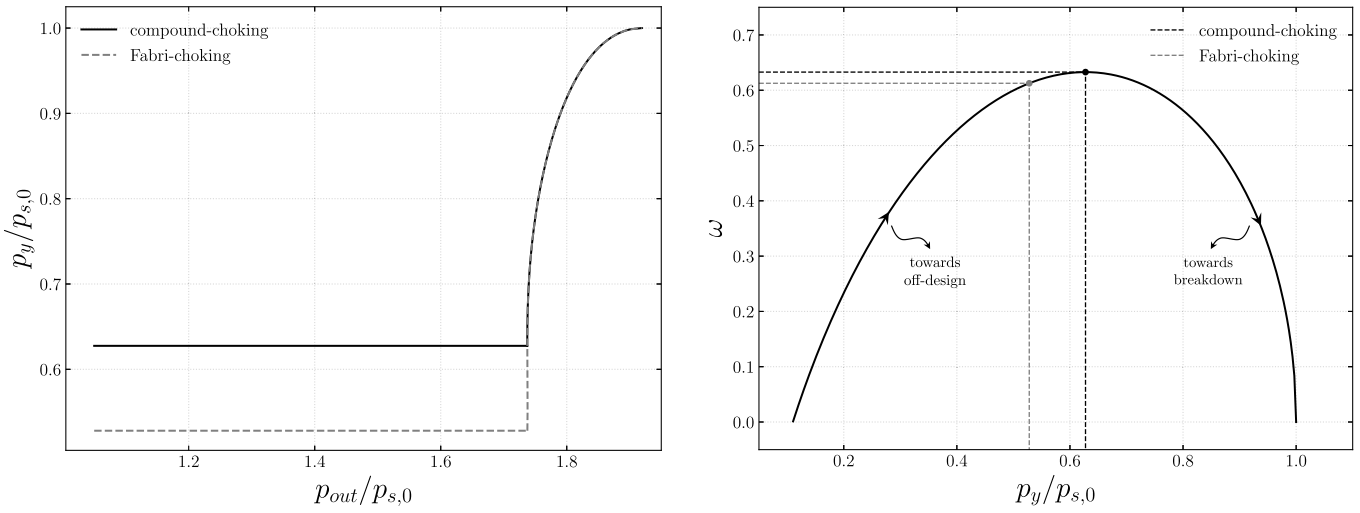

(a) $p_y/p_{s,0}$ vs $p_{out}/p_{s,0}$ (b) ω vs $p_y/p_{s,0}$

Fig. 6. Comparison between Fabri-choking and compound-choking for $p_{p,0}/p_{s,0} = 4.5$. The working fluid is air and $\eta_m = 0.92$. The positions of the critical conditions have been highlighted on the ω-curve.

of the critical back pressure. Note also that the off-design curves all have the same breakdown pressure. This is explained by the fact that at the breakdown pressure, $\dot{m}_s = 0$ and the secondary flow does not influence the total flow anymore. This is not true when η_p varies, which is why the breakdown pressures in Fig. 7a are not the same. Moreover, one can observe that the spurious overshoot that was previously discussed in the case of the Fabri-choking curves is also present in the compound-choking curves. This is actually due to the fact that, as explained in Croquer et *al.* [28], the compound-choking criterion as expressed in Eq. (11) is not rigorously correct if one considers non-isentropic flows. Indeed, because the criterion in Eq. (11) was obtained with the hypothesis of isentropic flow, when friction losses are introduced into the model by means of the isentropic efficiencies, Eq. (11) is no longer rigorously accurate, in the sense that the compound-choking indicator β is no longer calculated in compliance with its definition, given in Ref. [25]. If Eq. (11) is nonetheless utilized with non-unity η_s or $\eta_{p,y}$, as it is the case for the curves in Fig. 7b and c, the spurious overshoot will be present on the compound-choking curves as well because Eq. (11) will not predict the maximum secondary mass flow rate. However, it will actually be demonstrated in the next section that using a *corrected* expression of β does maximize the secondary mass flow rate. Therefore, when dealing with non-isentropic expansions, the correct choking criterion should be that the total mass flow rate is maximized, which is in concordance with Eq. (11), with the proper computation of β.

- Decreasing $\eta_{p,y}$ has a somewhat similar effect to decreasing η_s, but to a lesser extent. However, none of the two mass fluxes are directly hindered by this efficiency. An intuitive way to explain this is that, as $\eta_{p,y}$ gets lower, the primary flow is expanded less efficiently in the mixing chamber. Thus, friction hinders the primary flow expansion (the flow velocity is lower), so that the primary flow mixing area $A_{p,y}$ must get higher to maintain the mass flow rate. Conversely, the secondary flow mixing area $A_{s,y}$ gets lower, therefore decreasing the secondary mass flow rate and hence the entrainment ratio.
- Lowering η_m does not influence the on-design entrainment ratio, as the latter does not depend on the mixing. As η_m decreases, the critical back pressure decreases. Indeed, the friction interactions cause a loss of stagnation pressure, thereby lowering the back pressure. This is comparable to a Fanno flow.
- The effect of η_d is quite similar to that of η_m. Lowering η_d tends to decrease the critical back pressure.

At this stage, one chooses not to use the diffuser isentropic efficiency η_d for later calibration. Indeed, this efficiency has the same influence on the characteristic curves as η_m. Furthermore, in real ejectors, the diffuser is usually well designed, meaning that it can reasonably be assumed that the flow is isentropic.

3.3. Fitting to R134a ejector experimental data

To calibrate the characteristic curves for ejectors working with R134a, the experimental data of Garcia del Valle et *al.* [29] are used as reference. Three different geometries were presented in the original article. However, they differ only in shape; the areas at the sections of interest (Fig. 2) are equal. For this reason, only one ejector can be modeled using the present 0-D model. The relevant ejector dimensions are thus $D_t = 2.0$ [mm], $D_e = 3.0$ [mm] and $D_y = 4.8$ [mm]. The stagnation conditions for the experiments are $(T_{sat})_{p,0} = 84.38$ °C and $(T_{sat})_{s,0} = 10$ °C with a superheating of 10 °C. Superheating the vapour ensures that the flow does not condense within the ejector.

It was found that an accurate calibration could be performed by using only three parameters, that are, $\eta_p = 0.977$, $\eta_s = 0.89$ and $\eta_m = 0.813$. The value of $\eta_{p,y}$ is thus maintained to 1. Note that these values appear to be plausible for real ejectors. Indeed, the primary nozzle flow is almost isentropic and the secondary flow slightly less due to the more complex geometry. The most limiting factor remains the mixing efficiency.

Fig. 8 shows the results of the calibration, along with the CFD results obtained by Croquer et *al.* [28]. The model fits quite well the experimental data of Garcia del Valle et *al.* [29], even better than the CFD results that tend to overestimate the entrainment ratio.

It is now proposed to plot the characteristic curves for the ejectors of Hakkaki-Fard et *al.* [30] using the calibration parameters found for the ejector of Garcia del Valle et *al.* [29], with the aim of determining if the calibration stays accurate. The three ejector geometries and operating conditions that were tested experimentally

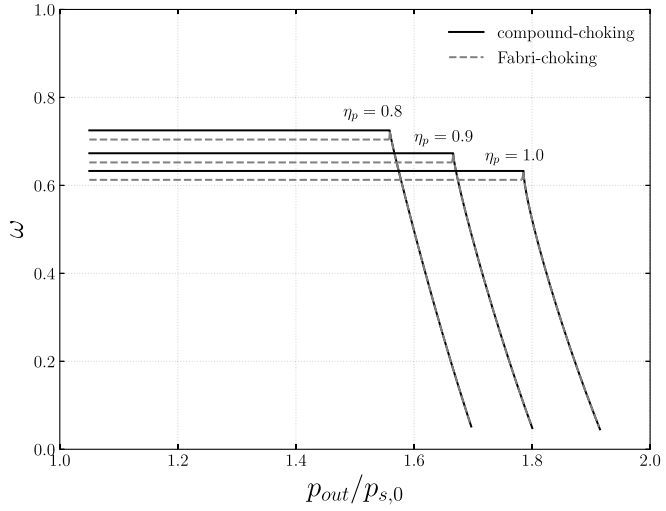

(a) Influence of η_p

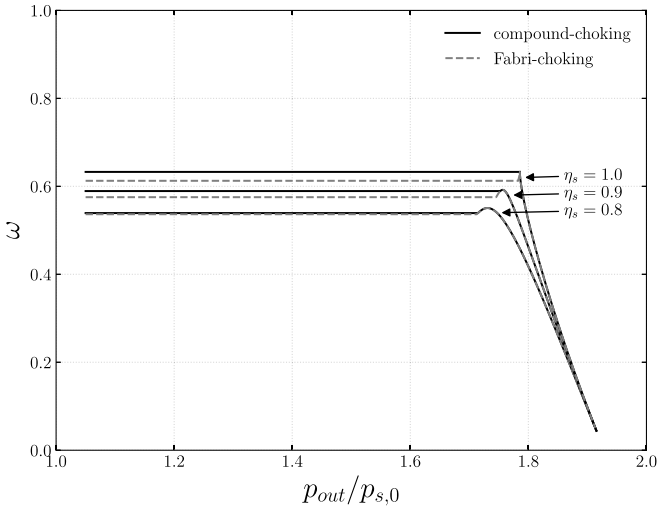

(b) Influence of η_s

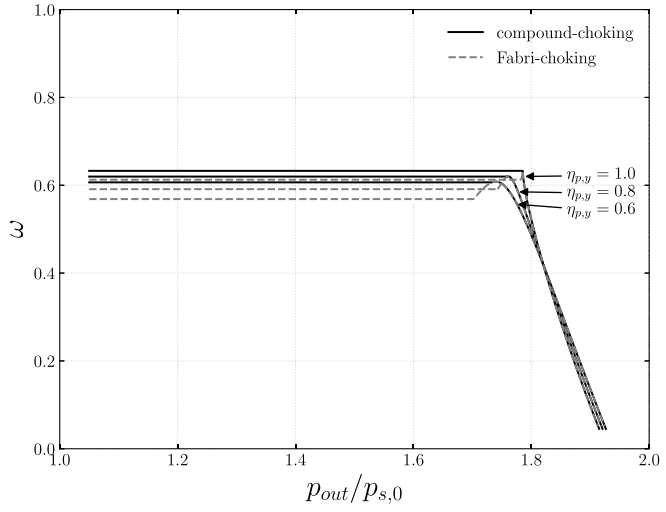

(c) Influence of $\eta_{p,y}$

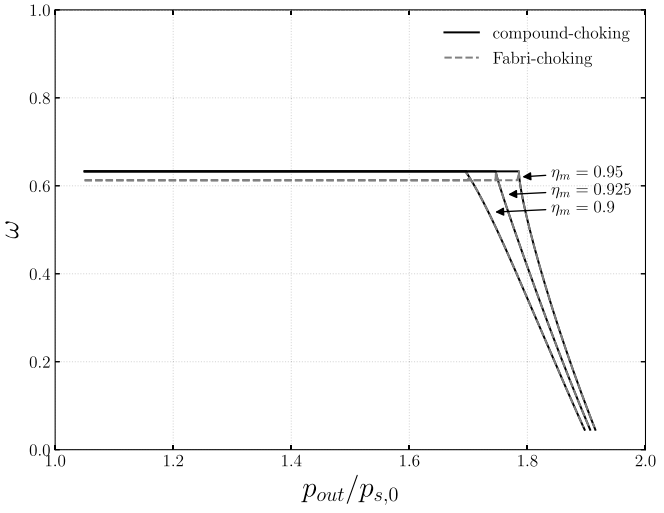

(d) Influence of η_m

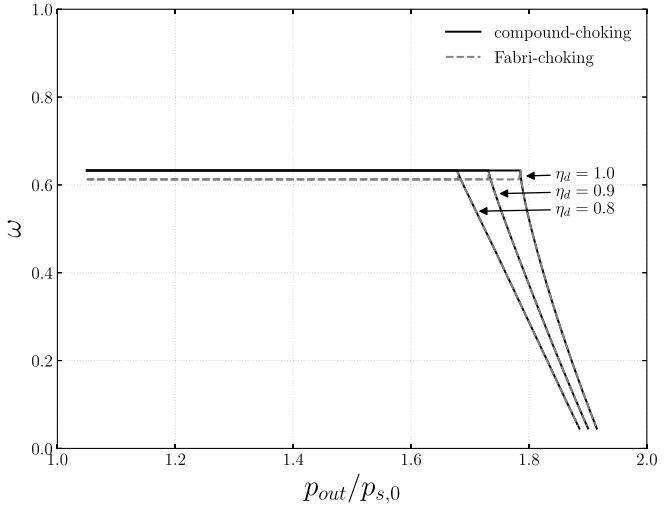

(e) Influence of η_d

Fig. 7. Influence of the different isentropic efficiencies on the characteristic curves using the compound-choking based model. The Fabri-choking model is also displayed for comparison purpose.

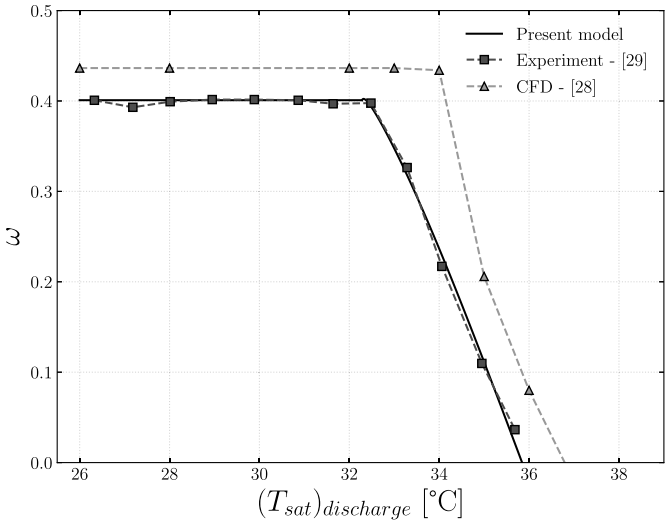

Fig. 8. Characteristic curve obtained for an ejector working with R134 with $(T_{sat})_{p,0} = 84.38$ °C, $(T_{sat})_{s,0} = 10$ °C, $\eta_p = 0.977$, $\eta_s = 0.89$ and $\eta_m = 0.813$. Comparison between the present numerical model, the CFD of Croquer et *al.* [28] and the experimental data of Garcia del Valle et *al.* [29].

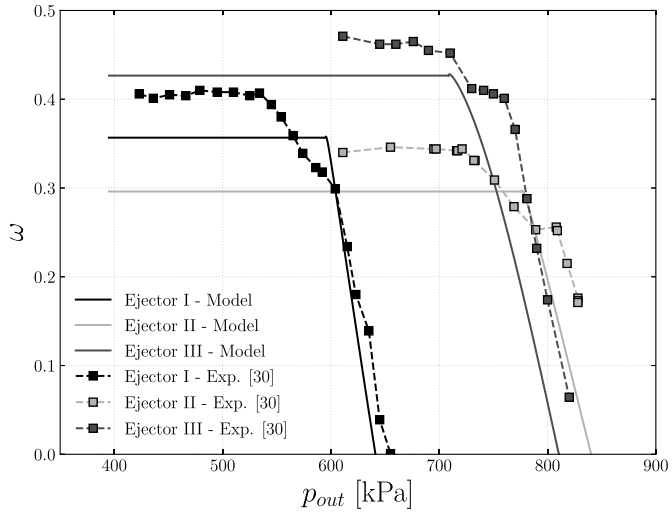

Fig. 9. Characteristic curves obtained for three ejectors working with R134 with $\eta_p = 0.977$, $\eta_s = 0.89$ and $\eta_m = 0.813$. Comparison between the present thermodynamic model and the experimental data of Hakkaki-Fard et *al.* [30].

are summarized in Table 1. Fig. 9 shows the results for the three ejectors. One can observe that, although the model does not predict the entrainment ratio as accurately as for the ejector of Garcia del Valle et *al.* [29], it nevertheless gives a good approximation. The model appears to underestimate the on-design entrainment ratio, but the off-design part of the characteristic curves seems to fit quite nicely. More precisely, the slopes of the off-design curves are quite accurate, and the model even overlaps the experiments for Ejector I. One could argue that the calibration process should yield better results if it were performed on one of the ejectors of Hakkaki-Fard et *al.* [30]. However, by doing so, the predictions of the characteristic curves for the two other ejectors were found to be quite poor, adding to the fact that the experimental curves of Hakkaki-Fard et *al.* [30] contain some rather unconventional double plateaus. Using the parameters obtained for the ejector of Garcia del Valle et *al.* [29] yields overall satisfactory predictions for the three ejectors of Hakkaki-Fard et *al.* [30].

3.4. Fitting to air ejector experimental data

The model was also calibrated on new experimental data obtained using the air ejector test bench at Université catholique de Louvain. As a reminder, the geometry of said ejector is given in the articles of Lamberts et *al.* [14,19].Again, the calibration could be performed by means of only three parameters, that are, $\eta_p = 0.977$, $\eta_s = 0.75$ and $\eta_m = 0.95$. As before, $\eta_{p,y}$ is set to 1. The relatively low value of η_s is likely to be caused by the peculiar geometry of the air ejector, adding to the fact that the secondary flow has to go through an angle of 90° before entering the mixing chamber (see Lamberts et *al.* [14] for more details about the ejector setup). On the other hand, the quite high mixing efficiency may reflect that the mixing process is relatively efficient. It should however be reminded that η_m is not an isentropic efficiency, therefore the mixing process will generate entropy even if said efficiency is set to unity.

Fig. 10 shows the fitting results obtained by calibrating the parameters on the new experimental data gathered for $p_{p,0}/p_{s,0} = 3.5$. Note that the secondary stagnation conditions correspond to the atmospheric ones for this particular ejector, so that $p_{s,0} = 1$ [bar]. In addition, the curves for $p_{p,0}/p_{s,0} = 2.5$ and $p_{p,0}/p_{s,0} = 4.5$, for which the values of the efficiencies have been kept equal to those previously mentioned, have also been displayed. One can see that the calibration allows the model to fit relatively well the experimental curves for the three cases. The off-design slopes do however not match the experimental data as well as for the case of Garcia del Valle et *al.* [29] seen previously. The error remains however limited, and the general shape of the curves is relatively close to that of the

Table 1
Geometry and operating conditions for the three experiments of Hakkaki-Fard et al. [30].

	Ejector I	Ejector II	Ejector III
Primary pressure $p_{p,0}$ [kPa]	2900	2633	1934
Primary temperature $T_{p,0}$ [°C]	106	100	86
Secondary pressure $p_{s,0}$ [kPa]	265	350	415
Secondary temperature $T_{s,0}$ [°C]	50	25	30
Primary throat diameter D_t [mm]	5.63	7.09	8.03
Primary nozzle exit diameter D_e [mm]	7.85	9.70	11.35
Mixing section diameter D_y [mm]	16.4	16.4	16.4

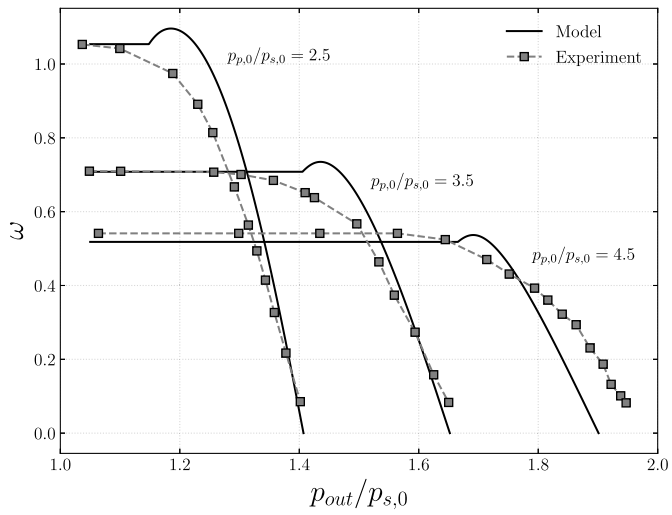

Fig. 10. Characteristic curves obtained for the air ejector test bench of Université catholique de Louvain with $\eta_p = 0.977$, $\eta_s = 0.75$ and $\eta_m = 0.95$. Comparison between the present thermodynamic model and new experimental data.

experimental ones. The main issue with those curves is that there is a significant spurious overshoot near the critical point.

4. Relation between the compound-choking criterion and the maximization of the mass flow rate

In this section, it is proposed to perform an analytical study on the compound-choking criterion in the frame of non-isentropic perfect gas flows. The aim is to demonstrate the connection between the compound-choking criterion and the maximization of the mass flow rate within an ejector, which could be put in parallel with the definition of choking in the classical sense, i.e. for a simple nozzle.

4.1. Non-isentropic nozzle flow of a perfect gas

Before going towards ejectors and multi-stream flows, one first needs to develop the equations for non-isentropic nozzle flows for perfect gases. The objective is to be able to determine the links between the differentials of all the physical quantities for such flows and the corresponding compound-choking criterion. In order to obtain an analytical solution for this problem, one will consider a polytropic efficiency, noted η_{pol} defined as:

$$\eta_{pol} = \frac{dh}{dh_{is}},$$

since one only deals with expansions. In the previous sections, isentropic efficiencies were used because these are more suited for global transformations. However, these two types of efficiencies (isentropic and polytropic) can be linked for an expansion of a perfect gas from pressure p_1 to p_2 through:

$$\eta = \frac{(p_2/p_1)^{\frac{(\gamma-1)\eta_{pol}}{\gamma}} - 1}{(p_2/p_1)^{\frac{\gamma-1}{\gamma}} - 1}. \tag{29}$$

The conservation equations in a control volume can be written as:

$$\frac{d\rho}{\rho} + \frac{dV}{V} + \frac{dA}{A} = 0, \tag{30}$$

$$\rho V dV + dp + 4\tau_w \frac{dx}{D_h} = 0, \tag{31}$$

$$dh_0 = dh + VdV = 0. \tag{32}$$

Combining the second Gibbs equation ($Tds = dh - \frac{1}{\rho}dp$) with Eq. (32), then Eq. (31) gives:

$$ds = \frac{1}{\rho T} 4\tau_w \frac{dx}{D_h}. \tag{33}$$

The same Gibbs equation can then be used for an isentropic process to successively get:

$$dh_{is} = \frac{1}{\rho} dp, \qquad \text{and} \qquad ds = \left(\eta_{pol} - 1\right) \frac{1}{\rho T} dp, \tag{34}$$

Combining Eqs. (33) and (34), one obtains:

$$4\tau_w \frac{dx}{D_h} = \left(\eta_{pol} - 1\right) dp.$$

The momentum equation thus becomes:

$$\rho V dV + \eta_{pol} dp = 0. \tag{35}$$

The pressure differential can be expressed as:

$$dp = \left(\frac{\partial p}{\partial \rho}\right)_s d\rho + \left(\frac{\partial p}{\partial s}\right)_\rho ds. \tag{36}$$

The first partial derivative is the definition of the speed of sound squared whereas, the second partial derivative needs more development. In the case of an isentropic flow, the second term is obviously equal to zero. Using the first Gibbs equation ($Tds = \frac{R}{\gamma-1} dT + pd\left(\frac{1}{\rho}\right)$) along with the perfect gas assumption, one can write:

$$ds|_\rho = \frac{R}{(\gamma-1)} \frac{dT}{T},$$
$$\frac{dp|_\rho}{p} = \frac{dT}{T}.$$

Using these two expressions, the second partial derivative of Eq. (36) can be written as:

$$\left(\frac{\partial p}{\partial s}\right)_\rho = \frac{p(\gamma-1)}{R},$$

and Eq. (36), combined with Eq. (34) then becomes:

$$dp = \frac{a^2}{1 - \left(\eta_{pol} - 1\right)(\gamma - 1)} d\rho. \tag{37}$$

Combining this last expression with the momentum equation (35) and the mass conservation equation (30), one obtains:

$$\frac{dV}{V}\left(\frac{1 - \left(\eta_{pol} - 1\right)(\gamma-1)}{\eta_{pol}} M^2 - 1\right) = \frac{dA}{A}, \tag{38}$$

where the definition of the Mach number $M = \frac{V}{a}$ was used. The Mach number differential can be linked to the velocity differential by:

$$\frac{dV}{V}\left(1 + \frac{\gamma-1}{2} M^2\right) = \frac{dM}{M}, \tag{39}$$

and one can finally obtain the differential equation linking the Mach number to the cross-section area:

$$\frac{dM}{M} \frac{\frac{1-(\eta_{pol}-1)(\gamma-1)}{\eta_{pol}} M^2 - 1}{1 + \frac{\gamma-1}{2} M^2} = \frac{dA}{A}. \tag{40}$$

The throat is defined as the location in the nozzle where $dA = 0$ and this last equation shows that this will occur for a Mach number $M_t = \sqrt{\frac{\eta_{pol}}{\eta_{pol} + \gamma(1-\eta_{pol})}}$ which is different from unity when $\eta_{pol} < 1$. This means that, as soon as the flow becomes non-isentropic, the flow does not reach sonic conditions at the throat when it is choked but somewhere further down the divergent. When the flow is considered to be non-isentropic, one can thus not use the unity Mach number at the throat as choking condition. This is in accordance with what was stated in Section 3.

4.2. Compound-choking criterion

One now considers a flow with several separate streams under the following assumptions:

1. The flow is one dimensional, steady-state and adiabatic.
2. There is no mixing between streams.
3. The pressure is constant between streams at each cross section.
4. The transverse pressure gradient caused by the streamline curvature is negligible.

Using the equations developed in the previous section, one can write, for each stream i:

$$\frac{dV_i}{V_i}\left(M_i^2\frac{1-\left(\eta_{pol,i}-1\right)(\gamma_i-1)}{\eta_{pol,i}}-1\right)=\frac{dA_i}{A_i}. \tag{41}$$

The momentum equation (35) expressed for each stream says that:

$$\rho_i V_i^2\frac{dV_i}{V_i}=-\eta_{pol,i}dp_i, \tag{42}$$

$$\Rightarrow -\eta_{pol,i}\frac{dp_i}{\rho_i V_i^2}A_i\left(M_i^2\frac{1-\left(\eta_{pol,i}-1\right)(\gamma_i-1)}{\eta_{pol,i}}-1\right)=dA_i. \tag{43}$$

Since one considers that the pressure and thus the pressure differential is identical for all streams and that $\sum_i \frac{dA_i}{dx}=\frac{dA}{dx}$, one obtains:

$$\begin{aligned}&\frac{1}{p}\frac{dp}{dx}\sum_i\frac{A_i}{\gamma_i M_i^2}\left(\eta_{pol,i}-M_i^2\left(1-\left(\eta_{pol,i}-1\right)(\gamma_i-1)\right)\right)\\&=\frac{dA}{dx}.\end{aligned} \tag{44}$$

One then defines the compound indicator β, similarly to what was done by Bernstein et *al.* [25], as:

$$\beta=\frac{\frac{dA}{dx}}{\frac{d(\ln(p))}{dx}}, \tag{45}$$

$$=\sum_i\frac{A_i}{\gamma_i M_i^2}\left[\eta_{pol,i}-M_i^2\left(1-\left(\eta_{pol,i}-1\right)(\gamma_i-1)\right)\right], \tag{46}$$

$$=\sum_i\frac{A_i}{\gamma_i}\left[\eta_{pol,i}\left(\frac{1}{M_i^2}-1\right)-\gamma_i(1-\eta_{pol,i})\right] \tag{47}$$

This expression can be verified to match the expression from Bernstein et *al.* [25] for the case $\eta_{pol,i}=1$. It can be shown through a compound wave analysis that this indicator must be equal to 0 for the compound flow to be choked.

4.3. Mass flow rate maximization for a supersonic ejector

From the compressible flow theory, when a flow is choked, its mass flow rate is maximized. Hence, if the compound-choking is the actual choking mechanism, it should be equivalent to maximizing the mass flow rate within the ejector. Since the primary mass flow rate is fixed, as the primary flow is itself choked in the primary nozzle, maximizing the mass flow rate in the ejector is equivalent to maximizing the secondary mass flow rate. The mass flow rate of the secondary flow in an ejector can be computed at the mixing section y using Eq. (12). Since the choking criteria (Fabri- or compound-choking) are destined at finding the pressure at the mixing section p_y such that the ejector is choked, the mass flow rate has to be maximized with respect to this pressure. One thus has:

$$\frac{\partial\dot{m}_s}{\partial p_y}=\frac{\dot{m}_s}{A_{s,y}}\left[\frac{1}{\rho_{s,y}}\frac{\partial\rho_{s,y}}{\partial p_y}A_{s,y}+\frac{1}{V_{s,y}}\frac{\partial V_{s,y}}{\partial p_y}A_{s,y}+\frac{\partial A_{s,y}}{\partial p_y}\right] \tag{48}$$

The area of the secondary stream at the mixing section $A_{s,y}$ is not known a priori but since $A_y=A_{p,y}+A_{s,y}$, one has $\frac{\partial A_{s,y}}{\partial p_y}=-\frac{\partial A_{p,y}}{p_y}$. Moreover, using the momentum equation (35), Eq. (48) becomes:

$$\frac{\partial\dot{m}_s}{\partial p_y}=\frac{\dot{m}_s}{A_{s,y}}\left[\frac{1}{\rho_{s,y}}\frac{\partial\rho_{s,y}}{\partial p_y}A_{s,y}-\frac{\eta_{pol,s}}{\rho_{s,y}V_{s,y}^2}A_{s,y}-\frac{\partial A_{p,y}}{\partial p_y}\right] \tag{49}$$

Using the definition of the primary mass flow rate and the momentum equation (35), the last partial derivative of the previous equation can be written as:

$$\frac{\partial A_{p,y}}{\partial p_y}=A_{p,y}\left[-\frac{1}{\rho_{p,y}}\frac{\partial\rho_{p,y}}{\partial p_y}+\frac{\eta_{pol,p}}{\rho_{p,y}V_{p,y}^2}\right] \tag{50}$$

Using this last relation as well as the link between the pressure and density differentials of Eq. (37), the derivative of the secondary mass flow rate with respect to the mixing pressure becomes:

$$\begin{aligned}\frac{\partial\dot{m}_s}{\partial p_y}=&\frac{\dot{m}_s}{A_{s,y}}\left[A_{s,y}\left(\frac{1-\left(\eta_{pol,s}-1\right)(\gamma_s-1)}{\rho_{s,y}a_{s,y}^2}-\frac{\eta_{pol,s}}{\rho_{s,y}V_{s,y}^2}\right)\right.\\&\left.+A_{p,y}\left(\frac{1-\left(-1_{pol,p}\right)\left(\gamma_p-1\right)}{\rho_{p,y}a_{p,y}^2}-\frac{\eta_{pol,p}}{\rho_{p,y}V_{p,y}^2}\right)\right],\end{aligned} \tag{51}$$

$$\begin{aligned}=&\frac{\dot{m}_s}{A_{s,y}p_y}\left[\frac{A_{s,y}}{\gamma_s}\left(\eta_{pol,s}\left(1-\frac{1}{M_{s,y}^2}\right)-\gamma_s\left(\eta_{pol,s}-1\right)\right)\right.\\&\left.+\frac{A_{p,y}}{\gamma_p}\left(\eta_{pol,p}\left(1-\frac{1}{M_{p,y}^2}\right)-\gamma_p\left(\eta_{pol,p}-1\right)\right)\right]\end{aligned} \tag{52}$$

This last expression can be compared to the expression of the compound-choking indicator β obtained in Eq. (47), taken for 2 streams at section y:

$$\frac{\partial\dot{m}_s}{\partial p_y}=-\frac{\dot{m}_s}{A_{s,y}\ p_y}\beta.$$

Thus it shows that applying the compound-choking criterion, i.e. $\beta=0$ to an ejector is similar to maximizing the total mass flow rate within this ejector. More fundamentally, this shows that the choking mechanism at play in a supersonic ejector is the compound-choking. Indeed, the flow within a device is choked if the mass flow rate is maximized. Since maximizing the mass flow rate and applying the compound-choking criterion yield the same result, both must be equivalent. Building on this conclusion, it is possible to correct the previously obtained characteristic curves, that were spoiled by the spurious overshoot caused by the faulty application of the compound-choking criterion when dealing with non-isentropic transformations within the mixing chamber (Section 4). Fig. 11 shows the corrected version of the characteristic

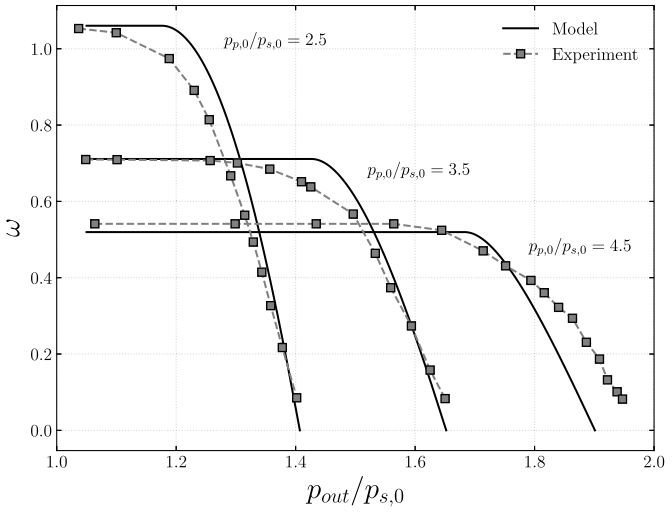

Fig. 11. Corrected characteristic curves obtained for the air ejector test bench at Université catholique de Louvain with $\eta_p = 0.977$, $\eta_s = 0.71$ and $\eta_m = 0.95$. Comparison between the present thermodynamic model and new experimental data.

curves displayed in Fig. 10. Obtaining the corrected curves is actually rather straightforward, as one only needs to locate the maximum of the overshoot (in this case, in Fig. 10), which indicates the location of the critical point and therefore of the on-design plateau. Note however that $\eta_s = 0.71$ in Fig. 11 for a better fitting of the experimental data.

5. Conclusion

In this paper, a new real gas thermodynamic model was presented. This model can be calibrated by means of multiple efficiencies. Although the model was only validated in the case of single-phase ejectors, it is foreseen to use this model for two-phase ejectors as well. This will be the subject of further studies.

First, a modified version of the model of Chen et *al.* [2] was implemented. As opposed to most models that can be found in the literature, this model uses the compound-choking criterion derived from the theory of Bernstein et *al.* [25], successfully applied to explain the choking mechanism in supersonic ejectors by Lamberts et al. [19,31], and further developed in the frame of real gas ejectors by Fang [26] and Metsue [27]. Rather than assuming constant mixing pressure and using a variable mixing efficiency as in the model of Chen et *al.* [2], the mass conservation equation was reintroduced into the mixing model. The decrease in performance in the off-design regime is thereby modeled by pressure effects within the constant area duct. The new model was then used to perform an analysis on the connections between the Fabri-choking and the compound-choking. Despite the fact that the Fabri-choking seems to be the most straight-forward approach to model ejector entrainment limitation, it actually does not lead to the maximization of the mass flow rate within the device, which is in contradiction with the definition of a choked flow.

After the determination of the individual impact of each calibration parameter, the model was validated for single-phase R134a (ejectors of Garcia del Valle et *al.* [29] and Hakkaki-Fard et *al.* [30]) and air (ejector of Université catholique de Louvain) flows. A good fitting ability was obtained for both fluids by using only three fitting parameters.

Lastly, an analytical study on the compound-choking criterion in the frame of non-isentropic perfect gas ejector flows showed that the use of the compound-choking criterion leads to the maximization of the total mass flow rate within the ejector. This is in accordance with the definition of choking for a simple nozzle (i.e. the maximization of the mass flow rate).

Future works include the validation of the present model for two-phase ejector predictions, especially those working with CO_2. The objective will be then to couple it to a model for a transcritical CO_2 heat pump and to assess the benefit of integrating an ejector on the performance of the whole cycle.

Declaration of competing interest

The authors declare that they have no known competing financial interests or personal relationships that could have appeared to influence the work reported in this paper.

Acknowledgements

A.M. and S.P. acknowledge the NSERC chair on industrial energy efficiency established in 2019 with the support of Hydro-Québec, Natural Resources Canada (CanmetEnergy-Varennes) and Emerson Commercial & Residential Solutions, which are here gratefully acknowledged.

References

[1] Besagni G. Ejectors on the cutting edge: the past, the present and the perspective. Energy 2019;170:998–1003. ISSN 0360-5442.
[2] Chen W, Shi C, Zhang S, Chen H, Chong D, Yan J. Theoretical analysis of ejector refrigeration system performance under overall modes. Appl Energy 2017;185:2074–84. ISSN 0306-2619.
[3] Rao S, Gopalan J. Observations on the non-mixed length and unsteady shock motion in a two dimensional supersonic ejector. Phys Fluids 2014;26:036103.
[4] Bouhanguel A, Desevaux P, Gavignet E. Flow visualization in supersonic ejectors using laser tomography techniques. Int J Refrig 2011;34(7):1633–40.
[5] Chen X, Omer S, Worall M, Riffat S. Recent developments in ejector refrigeration technologies. Renew Sustain Energy Rev 2013;19:629–51. ISSN 1364-0321.
[6] Besagni G, Mereu R, Inzoli F. Ejector refrigeration: a comprehensive review. Renew Sustain Energy Rev 2016;53:373–407. ISSN 1364-0321.
[7] Aidoun Z, Ameur K, Falsafioon M, Messaoud B. Current advances in ejector modeling, experimentation and applications for refrigeration and heat pumps. Part 1: single-phase ejectors. Inventions 2019;4:15.
[8] Aidoun Z, Ameur K, Falsafioon M, Messaoud B. Current advances in ejector modeling, experimentation and applications for refrigeration and heat pumps. Part 2: two-phase ejectors. Inventions 2019;4:16.
[9] Grazzini G, Milazzo A, Mazzelli F. Ejectors for efficient refrigeration: design, applications and computational fluid dynamics[M]. Springer; 2018.
[10] Keenan JH, Neumann EP, Lustwerk F. An investigation of ejector design by analysis and experiment. J Appl Mech 1950;72(17):299–309.
[11] He S, Li Y, Wang R. Progress of mathematical modeling on ejectors. Renew Sustain Energy Rev 2009;13(8):1760–80. ISSN 1364-0321.
[12] Munday JT, Bagster DF. A new ejector theory applied to steam jet refrigeration. Ind Eng Chem Process Des Dev 1977;16(4):442–9.
[13] Fabri J, Siestrunck R. Supersonic air ejectors. In: 5 of advances in applied mechanics. Elsevier; 1958. p. 1–34.
[14] Lamberts O, Chatelain P, Bartosiewicz Y. Numerical and experimental evidence of the Fabri-choking in a supersonic ejector. Int J Heat Fluid Flow 2018;69:194–209. ISSN 0142-727X.
[15] Eames I, Aphornratana S, Haider H. A theoretical and experimental study of a small-scale steam jet refrigerator. Int J Refrig 1995;18(6):378–86. ISSN 0140-7007.
[16] Huang B, Chang J, Wang C, Petrenko V. A 1-D analysis of ejector performance. Int J Refrig 1999;22(5):354–64. ISSN 0140-7007.
[17] Rogdakis E, Alexis G. Design and parametric investigation of an ejector in an air-conditioning system. Appl Therm Eng 2000;20(2):213–26. ISSN 1359-4311.
[18] Chen W, Liu M, Chong D, Yan J, Little AB, Bartosiewicz Y. A 1D model to predict ejector performance at critical and sub-critical operational regimes. Int J Refrig 2013;36(6):1750–61. ISSN 0140-7007.
[19] Lamberts O, Chatelain P, Bourgeois N, Bartosiewicz Y. The compound-choking theory as an explanation of the entrainment limitation in supersonic ejectors. Energy 2018;158:524–36. ISSN 0360-5442.
[20] Selvaraju A, Mani A. Analysis of an ejector with environment friendly refrigerants. Appl Therm Eng 2004;24(5):827–38. ISSN 1359-4311.
[21] Cizungu K, Groll M, Ling Z. Modelling and optimization of two-phase ejectors for cooling systems. Appl Therm Eng 2005;25(13):1979–94. ISSN 1359-4311.
[22] Ameur K, Aidoun Z, Ouzzane M. Modeling and numerical approach for the

design and operation of two-phase ejectors. Appl Therm Eng 2016;109:809–18. ISSN 1359-4311.
[23] Taslimi Taleghani S, Sorin M, Poncet S. Modeling of two-phase transcritical CO_2 ejectors for on-design and off-design conditions. Int J Refrig 2018;87:91–105. ISSN 0140-7007.
[24] Zegenhagen M, Ziegler F. A one-dimensional model of a jet-ejector in critical double choking operation with R134a as a refrigerant including real gas effects. Int J Refrig 2015;55:72–84. ISSN 0140-7007.
[25] Bernstein A, Heiser WH, Hevenor C. Compound-compressible nozzle flow. J Appl Mech 1967;34(3):548–54.
[26] Fang Y. Advanced numerical simulations of two-phase CO_2 ejectors. Ph.D. thesis. Université catholique de Louvain, Université de Sherbrooke; 2019.
[27] Metsue A. An improved thermodynamic model for supersonic ejectors. Master's thesis. Université catholique de Louvain; 2020.
[28] S. Croquer, Y. Fang, A. Metsue, Y. Bartosiewicz, S. Poncet, Compound-choking theory for supersonic ejectors working with real gas, Energy 227, ISSN 0360-5442.
[29] García del Valle J, Saíz Jabardo J, Castro Ruiz F, San José Alonso J. An experimental investigation of a R-134a ejector refrigeration system. Int J Refrig 2014;46:105–13. ISSN 0140-7007.
[30] Hakkaki-Fard A, Aidoun Z, Ouzzane M. A computational methodology for ejector design and performance maximisation. Energy Convers Manag 2015;105:1291–302. ISSN 0196-8904.
[31] Lamberts O. Choking and mixing phenomena in supersonic ejectors. Ph.D. thesis. Université Catholique de Louvain; 2018.